Nature of hydrogen defects in clinopyroxenes from room temperature up to 1000 °C: Implication for the preservation of hydrogen in the upper mantle and impact on electrical conductivity

Yan Yang, Jannick Ingrin, Qun-Ke Xia, Wendi Liu

1   Revision 2

2   **Nature of hydrogen defects in clinopyroxenes from room temperature up to 1000**
3   **^{o}C: Implication for the preservation of hydrogen in the upper mantle and impact**
4   **on electrical conductivity**

5   YAN YANG*[1], JANNICK INGRIN[2], QUNKE XIA[1], AND WENDI LIU[1]

6   [1]Institute of Geology and Geophysics, School of Earth Sciences, Zhejiang University, Hangzhou
7   310027, China
8   [2]Univ.Lille, CNRS, INRA, ENSCL, UMR 8207, UMET, Unité Matériaux et Transformations, F
9   59000 Lille, France
10   * Corresponding author
11   Institute of Geology and Geophysics
12   School of Earth Sciences
13   Zhejiang University
14   Hangzhou 310027, China

15   Email: yanyang2005@zju.edu.cn

16   **ABSTRACT**

17   Water incorporated as hydrogenated defects in mantle minerals can influence

18   physical properties of the mantle. Knowledge of hydrogen defects at high

19   temperatures (T) is fundamental to understand and quantify their influence on mantle

20   physical properties. Clinopyroxene contributes significantly to the upper mantle water

21   budget. Here, we investigate the behavior of hydrogen defects in ten natural

22   clinopyroxene crystals at temperatures up to 1000 ^{o}C, using *in situ* and quenched

23   experiments. The *in situ* high T Fourier transform infrared (FTIR) spectra indicate no

24   proton transfer between point defects, but the local environments of hydrogen defects

25   vary. Dehydration rates at 1000 ^{o}C of the six samples with different chemical

26   compositions are calculated based on the quenched experiments. These rates are not

27   only slightly site-specific, but also increase with Fe and tetrahedrally coordinated Al

28   contents. Indeed, the Near-FTIR spectra suggest that the dehydration of the samples in

29   this study involves oxidation of Fe^{2+}. For two diopsides with a mantle affinity, the

30   diffusivity is about 10^{-12} m^2/s at 1000 °C. The results mainly have the following

31   implications: (1) the different local environments of hydrogen defects between high T

32   and low T may be responsible for the different mechanism of water impact on

33   electrical conductivity between high and low T experiments; (2) since the hydrogen

34   diffusivities are positively related to Fe and ^{IV}Al contents, more care is required for

35   interpretation of measured water concentrations for clinopyroxene samples with high

36   Fe and ^{IV}Al contents. Compared between hydrogen diffusivities of olivine,

37   orthopyroxene and clinopyroxene in mantle peridotite, clinopyroxene should be the

38   most reliable recorder of water from depth.

39   **Keywords:** hydrogen defect, clinopyroxene, high temperature, diffusivity, *in situ*

40   FTIR, electrical conductivity, effect mechanism

INTRODUCTION

42   The main minerals in the deep earth are nominally anhydrous minerals (NAMs),

43   nevertheless, water can be incorporated as hydrogen defects which may strongly

44   influence physical properties of NAMs, such as electrical conductivity, rheology and

45   heat transferring (e.g., Mackwell et al. 1985; Karato 1990; Wang et al. 2006; Yoshino

46   et al. 2008; Thomas et al. 2012; Faul et al. 2016; Chang et al. 2017), thereby affecting

47   physical/chemical processes in the deep Earth (Peslier et al. 2010; Xia et al. 2013;

48   Demouchy and Bolfan-Casanova 2016; Liu et al. 2017). However, the importance of

49   water effect on several properties are still under current debates (e.g., Wang et al.

50   2006; Yoshino et al. 2006, 2008; Costa and Chakraborty 2008; Demouchy et al. 2012;

51   Jones et al. 2012; Fei et al. 2013; Karato and Wang 2013; Yoshino and Katsura 2013;

52   Dai and Karato 2015; Gardés et al. 2015). This is not only caused by differences in

53   experimental methods, but also due to the complications in speciation of hydrogen

54   defects (Karato 2015; Jones 2016). For instance, some recent experimental studies

55   have reported that different hydrogen defects in NAMs have different effects on

56   properties such as rheology and elasticity (e.g., Faul et al. 2016; Purevjav et al. 2016;

57   Padrón-Navarta and Hermann 2017; Tielke et al. 2017). As a result, understanding

58   speciation of hydrogen defects is fundamental to understand water effects on

59   properties of NAMs. Theoretically, Karato (2006) speculated that speciation and sites

60   of hydrogen defects in NAMs at high temperature may not be the same as those at

61   room temperature. In fact, several studies have indicated that speciation of hydrogen

62   defects at room temperature may be misleading for discussing physical mechanism of

63   water effects on properties of NAMs at high temperature. For example, Aines and

64   Rossman (1985) reported that water speciation in feldspar at high temperature was

65   different from that at room temperature. Yang and Keppler (2011) reported that

66   hydrogen defects assigned to Si vacancies in olivine were unstable with increasing

67   temperature. Yang et al. (2011) and Guo (2017) have reported that water speciation in

68   rutile at room temperature is not representative of that at high temperatures relevant

69   for subduction zones or upper mantle conditions. Yang et al. (2015) and Liu et al.

70   (2018) found unquenchable transferring of hydrogen defects between sites in

71   anorthoclase with increasing temperature. Very recently, Qin et al. (2018) has shown

72   by numerical modeling that water speciation in olivine could be influenced by

73   temperature and pressure. Consequently, knowledge of hydrogen defects in NAMs at

74   high temperatures is essential to understand if water effects on mantle physical

75   properties are significant at temperature and pressure conditions of Earth mantle.

76   In addition, different hydrogen defects have different diffusivities at high

77   temperature. Recent experimental studies have reported site-specific hydrogen

78   diffusivities for Ti-doped Fe-free olivine and clinopyroxene, respectively

79   (Padrón-Navarta et al. 2014; Ferriss et al. 2016). Those works provide bases for

80   distinguishing multiple processes in the history of an olivine grain (Tollan et al. 2015)

81   and permit evaluating if water observed in upper mantle minerals is representative of

82   the deep mantle (Denis et al. 2018). However, the recent study on naturally hydrated

83   olivine did not report drastic difference in diffusivities for various hydrogen defects

84   (Thoraval et al. 2018). Thus, the lack of consensus is a call for further study on

85   site-specific hydrogen diffusion, especially in clinopyroxene.

86   Indeed, clinopyroxene is one of the main constituent minerals in the lower crust

87   and upper mantle. Clinopyroxene is the pyroxene with large cations such as Ca^{2+},

88   Na^+ and Li^+ occupied in the M2 sites in the structure, thereby with space group C2/c

89   at ambient conditions. For example, the diopside-hedenbergite solid solution, augite,

90   jadeite, omphacite, spodumene and aegirine are clinopyroxene minerals. Among

91   them, the diopside and augite are calcic clinopyroxenes, jadeite, omphacite and

92   aegirine are sodic clinopyroxenes, while spodumene is lithium aluminum silicate.

93   Diopside is the main phase of the upper mantle peridotite. Hydrogen tends to

94   partition into it rather than olivine and orthopyroxene (e.g., Aubaud et al. 2004;

95   Grant et al. 2007; Demouchy et al. 2016). For diopside form mantle peridotite, water

96   content ranges from 0 to 1000 wt. ppm (Demouchy et al. 2016). In addition,

97   omphacite from mantle eclogite can contain water content up to 1800 ppm (Smyth et

98   al. 1991). Yang et al. (2010, 2015) investigated the behavior of hydrogen defects in

99   clinopyroxenes at temperatures between 20 and 500 °C. They found that the

100 speciation and sites of hydrogen defects did not change over the temperature range,

101 but the O-H bond stretching frequencies varied with different extent for different

102 hydrogen defects. To date, defects in clinopyroxene under temperatures

103 corresponding to the upper mantle remains unclear.

104 Consequently, in order to understand whether hydrogen defects observed at

105 ambient conditions reflect their behavior at mantle temperatures, we investigated

106 behavior of different hydrogen defects in clinopyroxenes at temperatures up to

107 1000 °C. Since nature of hydrogen defects is closely related to chemical environment,

108 we chose ten clinopyroxene samples with different compositions (calcic and sodic

109 clinopyroxenes, Fe-poor and Fe-rich clinopyroxenes) from various localities. We

110 measured *in situ* Fourier transform infrared (FTIR) spectra of ten clinopyroxenes to

111 monitor variations of hydrogen sites with increasing temperature. We also carried out

112 quenched experiment at 1000 °C to determine hydrogen diffusivity of different OH

113 groups. The Near-FTIR spectra of Fe^{2+} in the samples before and after dehydration

114 were collected to qualify the dehydration mechanism. Those results provide

115 information about what happens to hydrogen defects at atomic level during high

116 temperature process, and contribute to further understanding preservation of hydrogen

117 defects and their effect mechanisms on electrical conductivity at high temperatures.

118 **MATERIALS AND METHODS**

119 **Sample description**

4

120   Ten natural clinopyroxene single crystals from different localities were analyzed

121   in this study: two gem-quality diopsides from Austria (diopside-Austria, with about 17

122   wt. ppm water) and Russia (diopside-Russia) which are previously described in Ingrin

123   et al. (1989) and Andrut et al. (2007); a diopside in a marble xenolith from the Mount

124   Marcy anorthosite massif at the Cascade Slide, New York, USA (diopside-marble),

125   with 138 wt. ppm water reported in Johnson et al. (2002); two diopside crystals from

126   Aksu, China (diopside-Aksu1, diopside-Aksu2), with 44 wt. ppm water reported in

127   Shuai and Yang (2017); a diopside in peridotite xenolith hosted by Cenozoic basalt

128   from Jiande, Zhejiang, China (diopside-JD), with 573 wt. ppm water reported in Hao

129   et al. (2014); a diopside in peridotite xenolith (Mid-Atlantic Ridge) (diopside-deep sea,

130   with 529 wt. ppm water, unpublished data); two augite megacrysts hosted by

131   Cenozoic basalt from Yingfengling (augite-YFL) and Nushan (augite-NS), China,

132   with less than 1 wt. ppm water reported by Yang and McCammon (2012); an

133   omphacite from eclogites from the Roberts Victor kimberlite pipe, South Africa

134   (omphacite), with 639 wt. ppm water reported by Huang et al. (2014). The samples

135   are all C2/c clinopyroxenes (see the crystal structure data in the in the supplementary

136   material). All samples were un-oriented and double polished single crystals. The

137   samples with grain thickness ranging from 0.124 to 0.995 mm were used for the *in*

138   *situ* high temperature FTIR spectra measurements. The samples with grain thickness

139   ranging from 0.146 to 0.980 mm were used for the dehydration experiments.

Electron probe micro analyzer (EPMA)

141   The chemical compositions of the samples were determined using an EPMA

142   1600 (Shimadzu) electron microprobe at Zhejiang University (China). The analyses

143   were performed with a 15 kV accelerating voltage, 10 nA beam current and a 5 μm

144   beam diameter. Natural minerals were used as standards, and a program based on the

145   ZAF procedure was applied for data correction. Multi-point measurements were

146   conducted from core to rim of each mineral grain. The analyses demonstrate the

147   chemical homogeneity of the samples. Reproducibility of multi-point analysis is <1%

148   for elements with concentration >5% and <3% for elements with concentration >1%.

149   Based on the average chemical compositions, the calculated cations per 6 oxygen

150   atoms are listed in Table 1.

In situ Mid-FTIR spectroscopy

152   Unpolarized and polarized FTIR spectra in the frequency range 4000-1000 cm^{-1}

153   were collected using a Nicolet iS50 FTIR spectrometer coupled with a Continuμm

154   microscope at Zhejiang University (China). A KBr beam-splitter and a liquid

155   nitrogen-cooled MCT-A detector were used. A total of 128 scans were accumulated

156   for each spectrum at a 4 cm^{-1} resolution. The squared aperture size was set to 50×50

157   μm. Background was collected at every temperature. Spectra were collected on the

158   same selected area for each sample.

159   For the *in situ* high temperature measurements, the samples were placed on a Pt

160   foil with a hole of 1.5 mm in diameter or on a sapphire plate in a heating stage with

161   CaF$_2$ windows, equipped with a resistance heater and an S-type thermocouple. The

162   sample was heated in N$_2$. The sample temperature was determined with an uncertainty

163   of less than 1 °C. The temperature was increased from 20 to 1000 °C using a heating

164   rate of 15 °C/min. For every temperature step, except otherwise indicated, the dwell

165   time was 5 minutes.

Quenched dehydration experiments

167   We choose six clinopyroxene samples with different chemical composition for

168   dehydration experiments. The experimental conditions and sample thickness are listed

169   in Table 2. They were annealed in the heating stage at a desired temperature of 1000

170   °C for different hours, respectively. To avoid oxidation by the air, the heating stage

171   was purged with N$_2$ of high purity during the annealing. Then FTIR measurements

172   were carried out on the samples after quenching to room temperature.

Near-FTIR (NIR) spectroscopy

174   To investigate variations of Fe^{2+} in the samples before and after dehydration,

175   NIR spectra in the frequency range 12000-4000 cm^{-1} were collected using a Bruker

176 Vertex70 FTIR spectrometer coupled with a hyperion1000 microscope at Zhejiang

177 University (China). A CaF_2 beam-splitter and an InGaAs detector were used. A total of

178 64 scans were accumulated for each spectrum at a 4 cm^{-1} resolution. The squared

179 aperture size was set to 50×50 μm. Spectra were collected on the same selected area

180 for each sample.

Data analysis

182 For *in situ* experiment, to analyze site-specific temperature dependence of each

183 OH band in the samples, spectra were decomposed using the Peakfit v4.12 software.

184 Width, amplitude and frequency of every single band were adjustable to obtain the

185 best peakfitting. For several samples with broad and significantly overlapped bands,

186 we used OMNIC7.1 software to obtain the bulk integral absorbances, because

187 peakfitting may not be the best way to extract absorbances (Zhang et al. 2007).

188 For the quenched experiment, we applied OMNIC7.1 software to obtain the bulk

189 integral absorbance and calculate the bulk hydrogen diffusivity. Peakfit was used to

190 obtain the integral absorbance of each OH band and calculate the site-specific

191 hydrogen diffusivity. Based on dimensions of the samples, hydrogen diffusivities of

192 the bulk hydrogen defects and site-specific hydrogen defect were obtained using the

193 one-dimensional model of diffusion from Ingrin et al. (1995). In the calculation of OH

194 concentration ratio of the final to initial concentration as a function of heating time,

195 we used the ratio of the final to initial peak area, rather than the absolute water

196 concentration. The resulting dehydration data were listed in Table 2.

RESULTS

Hydrogen defects at ambient conditions

199 As commonly observed in natural clinopyroxene (e.g., Skogby et al. 1990), four

200 groups of OH absorption bands are found in the ten samples: 3620-3640 cm^{-1} (group

201 1), 3530-3540 cm^{-1} (group 2), 3460 cm^{-1} (group 3) and 3360 cm^{-1} cm^{-1} (group 4) as

202 shown in Figure 1. Not every OH band is prominent in all samples because of the

203 differences in thickness, chemical composition and crystallographic orientation of the

7

204   samples. Among the ten samples, the FTIR spectra of the diopside-Austria and

205   diopside-Russian, the diopside-marble, the diopside-Aksu have also been reported in

206   Ingrin et al. (1989), Johnson et al. (2002), Shuai and Yang (2017), respectively. It

207   should be noted that the band of group 1 at 3620-3640 cm^{-1} in omphacite may not be

208   intrinsic but related to nanometer-sized inclusions within the crystals (Koch-Müller et

209   al. 2004), thus we did not consider further this OH band of omphacite in the rest of the

210   study.

211   Cation substitutions usually cause shifts in band positions (Libowitzky and Beran

212   2006). Combined with the previously reported and some unpublished data of

213   clinopyroxene, positions of the OH bands of group 1 are plotted versus chemical

214   compositions in Figure 2. The band position correlates roughly with the amount of

215   tetrahedral coordinated Al^{3+} (^{IV}Al) (Fig. 2a, b). This supports the assignment of the

216   group 1 band to coupled substitution of Al^{3+} and H^+ in Si vacancy (e.g., Skogby et al.

217   1990; Bromiley and Keppler 2004; Gavrilenko et al. 2010). To date, the band of group

218   2 lacks a clear compositional association. Some studies suggested that it was related

219   to substitution of H in M2 site or coupled substitution of H with some lower valence

220   cations in M1 site (Skogby et al. 1990; Bromiley and Keppler 2004), while

221   Koch-Müller et al. (2004) assigned it again to coupled substitution of Al^{3+} and H^+ for

222   Si vacancy. Based on the relationship between OH frequencies and chemical

223   compositions, we further divide the group 2 OH band into the group 2a with OH

224   wavenumbers higher than 3535 cm^{-1} and the group 2b with OH wavenumbers lower

225   than 3535 cm^{-1} (Fig. 2b, c). The group 2a OH is related to tetrahedral coordinated Al^{3+},

226   which is consistent with the assignment in Koch-Müller et al. (2004). In agreement

227   with Skogby et al. (1990) and Bromiley and Keppler (2004), the group 2b OH could

228   be related to vacant M sites. Figure 2 also indicates that group 3 band may be related

229   to the vacant M site, consistent with the assignment of it to coupled substitution of H

230   and trivalent cation in M2 (Smyth et al. 1991; Koch-Müller et al. 2004; Stalder and

231   Ludwig 2007). The group 4 is rare in natural samples and only exists in the

232   diopside-Austria and diopside-Aksu2 in this study. These two diopsides have much

8

233 more M vacancies when compared to the others. It may be related to a higher M

234 vacancy concentration than in other samples, thus supporting the assignment of H

235 substitution in Mg vacancies (Stalder and Ludwig 2007). The negative vacancy may

236 be due to the presence of ferric iron (Fe^{3+}) in these samples, which we neglected in the

237 calculations. Indeed, the sample with the most negative vacancy is the Fe^{3+}-rich augite.

238 Yang and McCammon (2012) reported that the augite-NS contains 34% of the total Fe

239 as Fe^{3+}.

240 **Behavior of hydrogen defects at high temperatures**

241 **OH bands at elevated temperatures**

242 Figure 3 shows the unpolarized FTIR spectra of the clinopyroxenes at different

243 temperatures (see the polarized FTIR spectra in the supplementary material). With

244 increasing temperature, most bands gradually weaken, broaden and even diminish,

245 especially for the bands at lower frequencies. A new OH band around 3443 cm^{-1} also

246 appears in the spectra of the diopside-Austria and diopside-Aksu2 quenched from

247 1000 °C.

248 In Figure 4, site-specific band shifts with increasing temperature are reported.

249 With increasing temperature, the band of group 1 linearly shifts to lower

250 wavenumbers but to different extents for the studied samples, while the band of group

251 4 linearly shifts to higher wavenumbers. For most samples, the group 2 and group 3

252 bands significantly overlapped and disappeared at high temperatures, thus, we only

253 display the data of samples with the prominent group 2 and group 3 bands. With

254 increasing temperature, the group 2 and group 3 bands generally shift to lower

255 wavenumbers, but not linearly or as drastically as the group 1 band does. The group 3

256 band of the diopside-Austria and diopside-Aksu2 shifts to higher wavenumbers with

257 increasing temperature to 800 °C, then shift to lower wavenumbers.

258 Furthermore, there is a decrease in the absorption of the OH bands at elevated

259 temperatures, especially for the augite-YFL and omphacite with almost no absorption

260 at 1000 and 700 °C, respectively. Comparing between the FTIR spectra of the ten

261   samples before heated and after quenched from 1000 °C, it is clear that dehydration

262   has occurred during the heating process for most of the samples. In order to explore at

263   which temperature dehydration starts, we analyzed variations of the OH absorbances.

264   The evolution of the bulk integral absorbance of the OH bands with temperature is

265   shown in Figure 5. With increasing temperature, the bulk integral absorbance exhibits

266   little variation for the diopside-marble, while it displays a turning point with drastic

267   decrease at the temperature above 600 °C for the diopside-Austria, diopside-Aksu1,

268   diopside-JD, diopside-Russia, augite-YFL and augite-NS. In contrast, the turning

269   point appears earlier at 300 °C in the evolution of the bulk integral absorbance of OH

270   bands in the diopside-Aksu2 with temperature. Unfortunately, for most samples, the

271   OH bands significantly overlap at high temperatures. This impedes the accurate

272   analysis of absorbance of each OH band (Zhang et al. 2007). We choose the

273   diopside-Austria and diopside-Aksu2 with well separated OH bands and show their

274   site-specific evolution in Figure 5. The absorbances of the bands of group 1, group 3

275   and group 4 in the diopside-Austria keep steady, then drastically decrease at 700 ^{o}C.

276   For the diopsde-Aksu 2, the absorbances of the bands of group 3 and group 4 do not

277   change until increasing temperature to 500 and 700 ^{o}C, respectively, while the

278   absorbance of the group 2b band decrease first then increase with increasing

279   temperature to 700 ^{o}C.

280   **Hydrogen diffusivities at 1000°C**

281   To investigate dehydration at high temperature, we conducted dehydration

282   experiments at 1000 ^{o}C on six samples with different chemical compositions. The

283   evolutions of the FTIR spectra with annealing time are shown in Figure 6. The bulk

284   and site-specific diffusion coefficients were obtained by fitting the data using a

285   one-dimensional model of diffusion as in Ingrin et al. (1995) and reported in Table 2.

286   The hydrogen diffusion coefficient is different not only between samples, but also

287   between hydrogen defects in the same sample. For example, the bulk hydrogen

288   diffusivities are the slowest in the diopside-marble and diopside-Russia ($6-7 \times 10^{-13}$

289   m^{2}/s), moderate in the diopsides from mantle peridotite (diopside-deep sea and

10

290   diopside-JD) (1×10^{-12} m^2/s), and the fastest in the diopside-Austria and augite-NS

291   (6×10^{-12} m^2/s). Moreover, it seems that the site-specific hydrogen diffusivity is

292   following different order between samples. For the diopside-marble, the

293   diopside-Russia and the augite-NS, the diffusivity of hydrogen responsible for the OH

294   band in group 1 is lower than that of the group 2. However, it is a little faster than that

295   of the group 2 for the diopside-deep sea and diopside-JD. We have reported the bulk

296   and site-specific diffusion coefficients as a function of chemical composition of the

297   six samples in Figure 7. There are satisfying positive correlations between hydrogen

298   diffusivities and chemical compositions except for the diopside-Austria. The presence

299   of microscopic amphibole lamellae previously reported by Ingrin et al. (1989) in this

300   sample could be a reason for its abnormal behavior. The lamellae provide possible

301   shortcuts for diffusion. Excluding the diopside-Austria, the bulk and site-specific

302   hydrogen diffusivities increase with the Fe and ^{IV}Al contents. The diffusivity of the

303   group 1 OH is more correlated with ^{IV}Al content, while that of the group 2 OH is

304   more correlated with Fe content. The bulk hydrogen diffusivity is more correlated

305   with Fe than ^{IV}Al content. In contrast to the temperature dependence of O-H bond

306   strength, we did not find any clear relationship between hydrogen diffusivity and its

307   corresponding band frequency. Thus, the difference of chemical composition has

308   much more effect on hydrogen diffusivity than the peak-specific difference does.

309ᴛ Variation of Fe^{2+} in the samples before and after dehydration

310   To explore the dehydration mechanism, Figure 8 compares the NIR spectra of the

311   clinopyroxene samples before and after the dehydration experiments. The bands

312   around 10,500 and 9500 cm^{-1} are assigned to crystal field bands (CFB) due to d-d

313   transitions of Fe^{2+} at M1 and M2 sites, respectively (Rossi et al. 1987; Burns et al.

314   1993). After dehydration, the absorbances of Fe^{2+} at both M1 and M2 sites decrease

315   for the diopside-Austria and diopside-Russia, while only the absorbances of Fe^{2+} at

316   M2 sites decrease for the two diopsides from mantle peridotite and the augite-NS.

317   DISCUSSION

Variations of local environments of hydrogen defects with increasing temperature

318

319

320   The frequency of an OH band reflects the strength of O-H bond. The site-specific

321   frequency shift of OH bands in clinopyroxene with increasing temperature indicates

322   different local environments of the hydrogen defects within their structures. The

323   negative frequency shifts of the group 1 OH bands indicate temperature-induced

324   lengthening and weakening of O-H bonds. The positive frequency shifts of the group

325   4 OH bands suggest weakening of hydrogen bonds (H…O) with increasing

326   temperature, because weakening of hydrogen bonds will induce a relative

327   strengthening of the primary O-H bond (Nakamoto et al. 1955; Xu et al. 2013). The

328   moderate negative frequency shifts of the groups 2 and 3 OH bands may indicate the

329   simultaneous action of the lengthening of O-H and H…O bonds. One can speculate

330   on a possible correlation between the initial frequency and its temperature dependence.

331   We show the temperature dependence of OH frequency as a function of initial

332   frequency for the clinopyroxene samples in this study and also for several minerals

333   from previous studies for comparison in Figure 9a. A near linear relation exists

334   between the temperature dependence of OH frequencies and their frequency at room

335   temperature for silicate minerals. The room-temperature frequency corresponding to

336   the cut-off between the positive and negative shift is around 3400 cm^{-1}. The

337   low-temperature evolution of OH bands in forsterite also suggests this rough

338   relationship (Ingrin et al. 2013). However, as shown in Figure 9a, the results for rutile

339   do not lie along the trends probably due to the very different structures of silicate and

340   oxide minerals.

341   In contrast to the resolved OH bands at room temperature, the IR spectra at 1000

342   ^{o}C display only one broad band. The one broad band at high temperature can arise

343   from a statistical distribution across multiple sites or hydrogen disordering in the

344   clinopyroxene structure. Based on the relationship between OH frequency and O-O

345   distance (Libowitzky 1999), we can provide some constraints on the hydrogen

346   bonding environments of hydrogen defects at room temperature and at 1000 ^{o}C

347   (Figure 9b). For the group 1 OH with frequencies around 3571-3553 cm^{-1} at 1000 $^{\circ}$C,

348   the predicted O-O distance is about 3.0 Å. For the group 2 OH with frequencies

349   around 3510-3469 cm^{-1} at 1000 $^{\circ}$C, respectively, the predicted O-O distance is about

350   2.9 Å. For the group 3 OH with frequencies around 3476-3417 cm^{-1} at 1000 $^{\circ}$C, the

351   predicted O-O distance is about 2.9-2.8 Å. For the group 4 OH with frequencies

352   around 3398-3387 cm^{-1} at 700 $^{\circ}$C, the predicted O-O distance is about 2.8 Å.

353   Obviously, the O-O distances for the four groups OH at 1000 $^{\circ}$C are more centralized

354   than those observed at room temperature (Fig. 9c). Thus, the one broad band at high

355   temperature such as 1000 $^{\circ}$C is interpreted here as temperature-induced hydrogen

356   disordering across multiple bonding sites with similar O-O distances. Temperature or

357   pressure-induced hydrogen disordering was also expected in the structures of

358   wadsleyite and ringwoodite (Kohn et al. 2002; Panero et al. 2013).

359   **Site-specific thermal stability of the hydrogen defects**

360   According to the Beer-Lambert relationship, A = εct, absorbance of O-H

361   vibration relates to absorption coefficient of O-H, water concentration and sample

362   thickness (ε is the absorption coefficient, A the measured integrated absorbance, t the

363   sample thickness, and c the concentration of the molecule studied). Previous studies

364   have shown that dehydration in diopside and augite could be neglected during the

365   short heating process from room temperature to 500 °C (Yang et al. 2010, 2015).

366   Additionally, contribution of the variation in sample thickness can be neglected below

367   500°C based on the thermal expansion of clinopyroxene (Pandolfo et al. 2015).

368   Furthermore, *in situ* polarized FTIR spectra (see supplementary material) at elevated

369   temperature indicate that O-H orientation does not significantly change with

370   temperature. Thus, the slight variation before the turning point in the evolution of the

371   integral absorbance with temperature indicates temperature dependence of OH

372   absorption coefficient. According to Barron (1962), the absorption coefficient of a

373   fundamental vibration transition is proportional to the square of the change of dipole

374   moments. Extensive studies have suggested that absorbance coefficient of O-H in

375   glasses and hydrous minerals is temperature dependent (e.g., Keppler and

376 Bagdassarov 1993; Withers et al. 1999; Zhang et al. 2007, 2016; Tokiwai and

377 Nakashima 2010; Della Ventura et al. 2017). However, only few studies addressed

378 temperature dependence of absorption coefficient of O-H vibration of hydrogen

379 defects in NAMs (Yang et al. 2010, 2012, 2015).

380   In contrast to the slight variations at low temperatures, the dramatic decrease of

381 the integral absorbance above the turning point at higher temperatures is due to

382 dehydration. For most samples in this study, dehydration begins at temperatures above

383 600 °C. However, the diopside-Aksu2 starts dehydrating as early as 300 °C, while

384 hydrogen defects in the diopside-marble are the most stable with negligible

385 dehydration during the heating process. The dominant OH band belongs to the group

386 1 in the diopside-marble, while they belong to the groups 2, 3 and 4 in the

387 diopside-Aksu2. It seems that the bands of group 1 are more stable than the ones of

388 the other groups. Thus, it is expected that different hydrogen defects have distinct

389 thermal stability. Indeed, in the diopside-Aksu2, dehydration of the group 3 starts at

390 500 °C, while the group 2b starts dehydrating at 200 °C and then re-hydrates at

391 700 °C. Dehydration of the group 4 starts at 700°C, which may account for the

392 re-hydration of the group 2b. However, the group 1, group 3 and group 4 in the

393 diopside-Austria start dehydrating at the same temperature. It is generally accepted

394 that breaking of O-H bonds must occur during the dehydration. Therefore, we attempt

395 to explain the different thermal stabilities of the hydrogen defects using the

396 temperature dependence of O-H bond strength. Note that the O-H bond corresponding

397 to the group 1 OH bands weakens, while that related to the group 4 OH bands

398 strengthens with increasing temperature. Thus, it will be taken for granted that the

399 hydrogen defects of the group 1 are most unstable defects, which was never

400 demonstrated before. Consequently, the driving force for the dehydration remains

401 complex.

402 **Dehydration mechanism and origin of the band at 3443 cm^{-1}**

403   Similar to Ferriss et al. (2016), we found that different hydrogen defects have

404 different diffusivities. Ferriss et al. (2016) proposed that the hydrogen defects of the

14

405 group 2 OH band diffuse faster than those of the group 1 OH band based on their two

406 diopside samples. Based on the data in this study, we do not find a uniform behavior

407 of the diffusivities for different OH bands. In the diopside-marble, diopside-Russia

408 and augite-NS, the hydrogen defects of the group 2 OH diffuse faster than those of the

409 group 1, in agreement with Ferriss et al. (2016). However, in the two diopsides from

410 mantle peridotite, the hydrogen defects of the group 2 OH band diffuse slightly slower

411 than those of the group 1 OH band. But the difference between OH bands in

412 clinopyroxene is not by more than one order of magnitude, far less than in Ti-doped

413 Fe-free forsterite (Padrón-Navarta et al. 2014). In contrast, hydrogen diffusivities are

414 mainly controlled by chemical compositions of the samples. Consistent with previous

415 studies (Skogby and Rossman 1989; Ferriss et al. 2016), the bulk hydrogen

416 diffusivities increase with Fe content (a.p.f.u.). For the two diopsides from mantle

417 peridotites with Fe around 0.07-0.08 a.p.f.u., the bulk diffusivity is on the order of

418 10^{-12} at 1000 $^{\circ}$C, one order of magnitude slower than the prediction of Ferriss et al.

419 (2016). Contrary to Ferriss et al. (2016), we obtain a positive relationship between the

420 bulk hydrogen diffusivities and ^{IV}Al content based on our data. We can further find

421 relationships between site-specific hydrogen diffusivities and chemical compositions.

422 For example, the diffusivity of hydrogen defects related to the group 1 OH band is

423 more dependent on ^{IV}Al content, while that of the group 2 OH band is more

424 dependent on Fe content. Thus, for the augite samples with high Fe and high ^{IV}Al,

425 hydrogen defects diffuse very fast.

426   As for hydrogen diffusion mechanism, there are self-diffusion deduced from H-D

427 exchange experiment, chemical diffusion controlled by the mobility of polarons and

428 chemical diffusion controlled by the mobility of metal vacancies (Ingrin and

429 Blanchard 2006). Among them, the mobility of polarons involves the

430 oxidation-reduction of iron. In this study, the absorbances of Fe^{2+} decrease with

431 dehydration. Thus, the dehydration mechanisms of the clinopyroxene samples involve

432 oxidation of Fe^{2+}: $Fe^{2+} + OH^- = Fe^{3+} + O^{2-} + 1/2H_2$. That is just what we observed in

433 relationship between hydrogen diffusivity and Fe content. Strictly speaking, the view

15

434   that extraction of H is a linear function of iron is an oversimplification. In fact, what is

435   important is the number of Fe^{2+} available for the reaction. Based on the initial

436   absorbances of Fe^{2+} in these samples, the content of Fe^{2+} is positively related to the

437   bulk Fe content. Therefore, using bulk Fe content in this study does not significantly

438   change the main results.

439   The band at 3443 cm^{-1} is not common in natural diopsides, but it has been

440   previously observed in synthetic Fe- and Na-doped diopsides (Stalder and Ludwig

441   2007; Purwin et al. 2009). Based on the similar pleochroic behavior of the bands at

442   3360 and 3443 cm^{-1}, Purwin et al. (2009) assigned the band at 3443 cm^{-1} to a coupled

443   substitution of a ferric iron and a proton to two neighboring Mg vacancies. Skogby

444   and Rossman (1989) reported the new band around 3443 cm^{-1} appearing in the FTIR

445   spectra of diopside from India after heating in H_2 or air and ascribed it to the lower

446   frequency shift of the 3460 cm^{-1} band. Ferriss et al. (2016) also observed the increase

447   of the band around 3443 cm^{-1} in the FTIR spectra of Kunlun diopside and Jaipur

448   diopside after gently heating. They suggested that this additional hydrogen was taken

449   up from the surroundings in the furnace, or was originally present in hydrous

450   microinclusions, or initially distributed evenly among the various initial peaks. Thus,

451   the origin of this new band has not been elucidated. In this study, the new band at

452   3443 cm^{-1} only occurs in the FTIR spectra of the diopside-Austria and Aksu2

453   quenched from high temperatures. Moreover, the 3443 cm^{-1} band seems to have an

454   orientation similar to the band at 3460 cm^{-1} related to the group 3 (Figure 10b).

455   Therefore, the band at 3443 cm^{-1} could be assigned to a new hydrogen defect in M site.

456   To draw some relationships between this new hydrogen defect and hydrogen defects

457   corresponding to other OH bands, variations of integral absorbances of the

458   deconvoluted bands of the quenched sample with isothermal annealing time are

459   plotted in Figure 10. With annealing time, the integral absorbance of the 3443 cm^{-1}

460   band slightly increases, the integral absorbance of the 3467 cm^{-1} band shows little

461   variation, while those of the 3645 and 3359 cm^{-1} bands decrease. As a result, it is

462   unlikely that the hydrogen defect corresponding to the new band is related to

463 hydrogen defect corresponding to the 3467 cm^{-1} band. Since hydrogen defect

464 corresponding to the 3645 cm^{-1} band is located in Si site, it is most likely that the

465 3443 cm^{-1} band is related to hydrogen defect corresponding to 3359 cm^{-1} which is

466 located in M site. In contrast to other samples, only these two samples have the group

467 4 OH band at 3359 cm^{-1}, which also supports our conclusion. Since dehydration

468 mechanism of the diopside from Austria involved the oxidation of Fe^{2+} to Fe^{3+}, the

469 3443 cm^{-1} band could be a new hydrogen defect in M site, coupled with the ferric iron

470 formed during dehydration, in agreement with Purwin et al. (2009).

471 **IMPLICATIONS**

472 **Hydrogen speciation and sites in the clinopyroxene at high temperatures: effect**

473 **mechanism on electrical conductivity**

474 It is well established that hydrogen defects can influence electrical conductivity

475 of their host minerals. However, there are discrepancies among published

476 experimental results (e.g., Wang et al. 2006; Yoshino et al. 2006, 2008; Karato and

477 Wang 2013; Yoshino and Katsura 2013). In view of these long standing discrepancies,

478 Karato (2013, 2015) proposed a new theoretical model and suggested that the

479 rate-controlling diffusing species of hydrogen-assisted electrical conductivity are

480 different from those of H-D isotopic exchange. This model provides a good

481 explanation of some discrepancies among the different experimental observations at

482 different temperatures. Moreover, Dai and Karato (2014) showed by experiment that

483 the mechanism of electrical conductivity of olivine changed with temperature, which

484 is also observed for mantle clinopyroxene by Zhao and Yoshino (2016). Based on the

485 model of Karato (2013), they proposed that the diffusion of protons in M site is the

486 dominant contribution to electrical conductivity at high temperatures, while free

487 protons at low temperatures. Although these results are well explained by the model

488 (Karato 2013), there has been no direct observation of the changes of free protons at

489 low temperatures to two protons in M site at high temperatures.

490 FTIR spectra are good tracers for local environments of hydrogen defects. From

491 the *in situ* FTIR spectra at elevated temperatures in this study, we do not find a

492 coupled growth and decline of OH bands as in rutile, anorthoclase or talc (Zhang et al.

493 2006; Yang et al. 2011, 2015; Guo 2017). This suggests that protons do not transfer

494 easily between sites in the clinopyroxenes with increasing temperature up to 1000 ^{o}C.

495 However, the local environments of hydrogen defects change with increasing

496 temperature. At high temperatures, the four groups of hydrogen defects have similar

497 O-O distances and display disordering in the structure. In contrast, the four groups of

498 hydrogen defects have distinct O-O distances and show ordering in the structure at

499 room T. Thus, it is unlikely that the water-effect on physical properties at high T is the

500 same as that as low T. At high T, the strength of bonding between protons and the

501 surrounding atoms are similar among the four groups of hydrogen defects. The

502 protons belonging to the four groups of hydrogen defects likely have similar mobility

503 at high T; this is likely not the case at low T. Therefore, the different local

504 environments of hydrogen defects between high T and low T can be responsible for

505 the different activation enthalpy of electrical conductivity between high and low T

506 experiments observed by Dai and Karato (2014) and Zhao and Yoshino (2016). In

507 addition, the pleochroism of hydrogen defects at high temperatures is not as

508 prominent as at room temperature (see supplementary material). Thus, it can be

509 inferred that anisotropy in electrical conductivity of clinopyroxene is also different

510 between high and room temperature, which deserves to be tested in the future work.

511 This study extends the understanding of hydrogen speciation and sites in

512 clinopyroxene at temperatures relevant to the lower crust and upper mantle. As

513 conditions relevant of the deep Earth involve both high pressure and high T, the local

514 environments of hydrogen defects in clinopyroxene at geologic conditions is

515 simultaneously constrained by high pressure and high temperature. To date, no data

516 have been reported for the high pressure behavior of hydrogen defects in

517 clinopyroxene. Previous *in situ* high pressure spectroscopic investigations on olivine,

518 wadsleyite and ringwoodite indicated that effect of pressure on variation in O-H bond

519 strength is the contrary to the temperature effect (Cynn and Hofmeister 1994;

520 Jacobsen et al. 2005; Chamorro Pérez et al. 2006; Koch-Müller et al. 2011; Panero et

521 al. 2013; Yang et al. 2014; Sakurai et al. 2015). Thus, it may be inferred the local

522 environments of hydrogen defects in clinopyroxene at high temperature and high

523 pressure is the same as ambient conditions. To fully address behavior of hydrogen

524 defects in clinopyroxene under deep earth conditions, simultaneous *in situ* high

525 temperature and high pressure FTIR spectroscopic investigations have to be carried

526 out.

Preservation of hydrogen speciation and content in quenched clinopyroxene

528 Our *in situ* heating experiments indicate that hydrogen speciation in

529 clinopyroxene does not change at least before dehydration. However, the dehydration

530 experiments by quenching induced slight modifications of hydrogen speciation. In this

531 case, a new band appears at 3443 cm^{-1}, which is linked to the dehydration process

532 involving the oxidation of iron. Therefore, the occurrence of this band if observed in

533 some natural clinopyroxenes could be used as a marker of a previous dehydration in

534 oxidizing conditions.

535 The hydrogen diffusivities are positively related to Fe and ^{IV}Al contents in the

536 clinopyroxene samples. Thus, for clinopyroxene samples with high Fe and ^{IV}Al

537 contents, more care is required for interpretation of measured water concentrations.

538 Based on the existing diffusivities of hydrogen in olivine and pyroxene, Denis et al.

539 (2018) concluded that the remaining hydrogen concentrations observed in peridotites

540 might only represent the "tip of the iceberg" of the water stored in the Earth's upper

541 mantle. However, the hydrogen diffusivity in mantle-derived clinopyroxene was not

542 available yet for referring in Denis et al. (2018). We provide here for the first time the

543 hydrogen diffusivity at 1000 ^{o}C in the mantle-derived diopside, and we show that its

544 diffusion coefficient may be one order of magnitude lower than that used in Denis et

545 al. (2018). For the hydrogen diffusivity controlled by the proton-vacancy mechanism,

546 it is similar and range between the diffusivities of olivine, enstatite and diopside, e.g.,

547 6×10^{-12}, 1.3×10^{-11}, and 3.1×10^{-11} m^2/s at 1100°C, respectively (Demouchy and

548 Mackwell 2006; Carpenter Woods 2001; Ferriss et al. 2016). The similar diffusivities

19

549 cannot explain the mineral specific hydrogen concentrations in the mantle xenoliths.

550 Therefore, the hydrogen diffusivity controlled by the proton-polaron mechanism may

551 in fact contribute to a different preservation of hydrogen in the olivine, enstatite and

552 diopside. In this study, the hydrogen diffusivity in the diopside samples is controlled

553 by the proton-polaron mechanism. It ranges between 1×10^{-12} and 1.2×10^{-12} m^2/s at

554 1000 ^{o}C in the two diopsides from mantle peridotites, two orders of magnitude lower

555 than 4×10^{-10} m^2/s in mantle olivine (Mackwell and Kohlstedt 1990), and slightly lower

556 than 4×10^{-12} m^2/s in mantle enstatite (Carpenter Woods 2001) at the same temperature.

557 It should be noted that the dehydration experiment in this study is carried out in open

558 system and ambient pressure, thus, the hydrogen diffusivity may be lower than 10^{-12}

559 m^2/s at 1000 ^{o}C in a closed system. As a result, clinopyroxene should be the most

560 reliable recorder of water from depth compared with the mantle olivine and

561 orthopyroxene, which was already inferred by Tian et al. (2016). Moreover, this study

562 shows that the hydrogen diffusivity of the group 1 OH (3620-3640 cm^{-1}) increases

563 with ^{IV}Al content, and that of the group 2 OH (3530-3540 cm^{-1}) increase with Fe

564 content. For the two diopsides from mantle peridotites, the hydrogen diffusivity at

565 1000 ^{o}C of the group 1 OH (3640 cm^{-1}, with the hydrogen diffusivity of 1.6×10^{-12}) is

566 slightly higher than that of the group 2 OH (3540 cm^{-1}, with the hydrogen diffusivity

567 of 1.2×10^{-12}). This site-specific difference is quite low and much less than the

568 difference caused by chemical composition. Therefore, preservation of water in

569 mantle clinopyroxene mainly depends on chemical composition.

ACKNOWLEDGMENTS

REFERENCES

20

578 Aines, R.D., and Rossman, G.R. (1985) The high temperature behavior of trace
579   hydrous components in silicate minerals. American Mineralogist, 70, 1169-1179.

580 Andrut, M., Wildner, M., Ingrin, J., and Beran, A. (2007) Mechanisms of OH defect
581   incorporation in naturally occurring, hydrothermally formed diopside and jadeite.
582   Physics and Chemistry of Minerals, 34, 543-549.

583 Aubaud, C., Hauri, E.H., and Hirschmann, M.M. (2004) Hydrogen partition
584   coefficients between nominally anhydrous minerals and basaltic melts.
585   Geophysical Research Letters, 31 (20).

586 Barrow, G.M. (1962) Introduction to molecular spectroscopy. Mc-Graw-Hill, New
587   York, 76-80.

588 Bromiley, G.D., and Keppler, H. (2004) An experimental investigation of hydroxyl
589   solubility in jadeite and Na-rich clinopyroxenes. Contributions to Mineralogy
590   and Petrology, 147, 189-200.

591 Burns, R.G. (1993) Mineralogical applications of crystal field theory, 2nd edn.
592   Cambridge University Press, Cambridge.

593 Carpenter Woods, S. (2001) The Kinetics of Hydrogen Diffusion in Single Crystal
594   Orthopyroxene. (PhD thesis). Dept. Geosciences. Pennsylvania State University.

595 Chamorro Pérez, E.M., Daniel, I., Chervin, J.C., Dumas, P., Bass, J.D., and Inoue, T.
596   (2006) Synchrotron IR study of hydrous ringwoodite (γ-Mg_2SiO_4) up to 30 GPa.
597   Physics and Chemistry of Minerals, 33, 502-510.

598 Chang, Y.Y., Hsieh, W.P., Tan, E., and Chen, J.H. (2017) Hydration-reduced lattice
599   thermal conductivity of olivine in Earth's upper mantle. Proceedings of the
600   National Academy of Sciences of the United States of America, 114, 4078.

601 Costa, F., and Chakraborty, S. (2008) The effect of water in Si and O diffusion rates in
602   olivine and implications for the transport properties and processes in the upper
603   mantle. Physics of the Earth and Planetary Interiors, 166, 11-29.

604 Cynn, H., and Hofmeister, A.M. (1994) High-pressure IR spectra of lattice modes and

605   OH vibrations in Fe-bearing wadsleyite. Journal of Geophysical Research, 99,
606   17717-17727.

607 Dai, L., and Karato, S. (2014) High and highly anisotropic electrical conductivity of
608   the asthenosphere due to hydrogen diffusion in olivine. Earth and Planetary
609   Science Letters, 408, 79-86.

610 Dai, L., and Karato, S. (2015) Reply to comment on "High and highly anisotropic
611   electrical conductivity of the asthenosphere due to hydrogen diffusion in olivine"
612   by Dai and Karato [Earth Planet. Sci. Lett. 408 (2014) 79-86]. Earth and
613   Planetary Science Letters, 427, 300-302.

614 Della Ventura, G., Susta, U., Bellatreccia, F., Marcelli, A., Redhammer, G.J., and
615   Oberti, R. (2017) Deprotonation of Fe-dominant amphiboles: Single-crystal
616   HT-FTIR spectroscopic studies of synthetic potassic-ferro-richterite. American
617   Mineralogist, 102, 117-125.

618 Demouchy, S., and Mackwell, S. (2006) Mechanisms of hydrogen incorporation and
619   diffusion in iron-bearing olivine. Physics and Chemistry of Minerals, 33,
620   347-355.

621 Demouchy, S., Tommasi, A., Barou, F., Mainprice, D., and Cordier, P. (2012)
622   Deformation of olivine in torsion under hydrous conditions. Physics of the Earth
623   and Planetary Interiors, 202-203, 75-70.

624 Demouchy, S., and Bolfan-Casanova, N. (2016) Distribution and transport of
625   hydrogen in the lithospheric mantle: A review. Lithos, 240-243, 402-425.

626 Demouchy, S., Thoraval, C., Bolfan-Casanova, N., and Manthilake, G. (2016)
627   Diffusivity of hydrogen in iron-bearing olivine at 3 GPa. Physics of the Earth
628   and Planetary Interiors, 260, 1-13.

629 Denis, C.M.M., Demouchy, S., and Alard, O., (2018) Heterogeneous hydrogen
630   distribution in orthopyroxene from veined mantle peridotite (San Carlos,
631   Arizona): Impact of melt-rock interactions. Lithos, 302-303, 298-311.

632 Faul, U., Cline, C.J., David, E.C., Berry, A.J., and Jackson, I. (2016)
633   Titanium-hydroxyl defect-controlled rheology of the Earth's upper mantle. Earth

22

634   and Planetary Science Letters, 452, 227-237.

635   Fei, H., Wiedenbeck, M., Yamazaki, D., and Katsura, T. (2013) Small effect of water

636   on uppermantle rheology based on silicon self-diffusion coefficients. Nature,

637   213-215.

638   Ferriss, E., Plank, T., and Walker, D. (2016) Site-specific hydrogen diffusion rates

639   during clinopyroxene dehydration. Contributions to Mineralogy and Petrology,

640   171, 1-24.

641   Gardés, E., Gaillard, F., and Tarits, P. (2015) Comment to "High and highly

642   anisotropic electrical conductivity of the asthenosphere due to hydrogen

643   diffusion in olivine" by Dai and Karato [Earth Planet. Sci. Lett. 408 (2014)

644   79-86]. Earth and Planetary Science Letters, 427, 296-299.

645   Gavrilenko, P., Ballaran, T.B., and Keppler, H. (2010) The effect of Al and water on

646   the compressibility of diopside. American Mineralogist, 95, 608-616.

647   Grant, K., Ingrin, J., Lorand, J.P., and Dumas, P. (2007) Water partitioning between

648   mantle minerals from peridotite xenoliths. Contributions to Mineralogy and

649   Petrology, 154 (1), 15-34.

650   Guo, H. (2017) In-situ infrared spectra of OH in rutile up to 1000°C. Physics and

651   Chemistry of Minerals, DOI 10.1007/s00269-017-0881-6.

652   Hao, Y.T., Xia, Q.K., Li, Q.W., Chen, H., and Feng, M. (2014) Partial melting control

653   of water contents in the Cenozoic lithospheric mantle of the Cathaysia block of

654   South China. Chemical Geology, 380, 7-19.

655   Hao, Y.T., Xia, Q.K., Jia, Z.B., Zhao, Q.C., Li, P., Feng, M., and Liu, S.C. (2016)

656   Regional heterogeneity in the water content of the Cenozoic lithospheric mantle

657   of Eastern China. Journal of Geophysical Research-solid Earth, 121, 517-537.

658   Huang, J.X., Li, P., Griffin, W.L., Xia, Q.K., Greau, Y., Pearson, N.J., and O'Reilly,

659   S.Y. (2014) Water contents of Roberts Victor xenolithic eclogites: primary and

660   metasomatic controls. Contributions to Mineralogy and Petrology, 168, 1092.

661   Ingrin, J., Latrous, K., Doukhan, J.C., and Doukhan, N. (1989) Water in diopside: An
662   electron microscopy and infrared spectroscopy study. European Journal of
663   Mineralogy, 1, 327-341.

664   Ingrin, J., Hercule, S., and Charton, T. (1995) Diffusion of hydrogen in diopside:
665   Results of dehydration experiments. Journal of Geophysical Research, 100,
666   15489-15499.

667   Ingrin, J., and Blanchard, M. (2006) Diffusion of Hydrogen on Minerals. Review of
668   Mineralogy & Geochemistry, 62, 291-320.

669   Ingrin, J., Liu, J., Depecker, C., Kohn, S.C., Balan, E., and Grant, K.J. (2013)
670   Low-temperature evolution of OH bands in synthetic forsterite, implication for
671   the nature of H-defects at high pressure. Physics and Chemistry of Minerals, 40,
672   499-510.

673   Jacobsen, S.D., Demouchy, S., Frost, D.J., Ballaran, T.B., and Kung, J. (2005) A
674   systematic study of OH in hydrous wadsleyite from polarized FTIR spectroscopy
675   and single-crystal X-ray diffraction: Oxygen sites for hydrogen storage in Earth's
676   interior. American Mineralogist, 90, 61-70.

677   Johnson, E.J., Rossman, G.R., Dyar, M.D., and Valley, J.W. (2002) Correlation
678   between OH concentration and oxygen isotope diffusion rate in diopsides from
679   the Adirondack mountains New York. American Mineralogist, 87, 899-908.

680   Jones, A.G., Fullea, J., Evans, R.L., and Muller, M.R. (2012) Water in cratonic
681   lithosphere: calibrating laboratory-determined models of electrical conductivity
682   of mantle minerals using geophysical and petrological observations.
683   Geochemistry Geophysics Geosystems, 13, 360-366.

684   Jones, A. (2016) Proton conduction and hydrogen diffusion in olivine: an attempt to
685   reconcile laboratory and field observations and implications for the role of grain
686   boundary diffusion in enhancing conductivity. Physics and Chemistry of
687   Minerals, 43, 237-265.

688   Karato, S. (1990) The role of hydrogen diffusivity in the electrical conductivity of the
689   upper mantle. Nature, 347, 272–273.

690   Karato, S. (2006) Influence of hydrogen-related defects on the electrical conductivity

691   and plastic deformation of mantle minerals: a critical review. In Earth's Deep

692   Water Cycle vol. 168, American Geophysical Union, Washington D.C.

693   Karato, S. (2013) Theory of isotope diffusion in a material with multiple species and

694   its implications for hydrogen-enhanced electrical conductivity in olivine. Physics

695   of Earth Planetary Interiors, 219, 49-54.

696   Karato, S., and Wang, D. (2013) Electrical conductivity of minerals and rocks. In:

697   Karato, S. (Ed.), Physics and Chemistry of the Deep Earth. Wiley-Blackwell,

698   New York, pp. 145-182.

699   Karato, S. (2015) Some notes on hydrogen-related point defects and their role in the

700   isotope exchange and electrical conductivity in olivine. Physics of the Earth and

701   Planetary Interiors, 248, 94-98.

702   Keppler, H., and Bagdassarov, N.S. (1993) High-temperature FTIR spectra of H_2O in

703   rhyolite melt to 1300 °C. American Mineralogist, 78, 1324-1327.

704   Koch-Müller, M., Matsyuk, S., and Wirth, B. (2004) Hydroxyl in omphacites and

705   omphacitic clinopyroxenes of upper mantle to lower crystal origin beneath the

706   Siberian platform. American Mineralogist, 89, 921-931.

707   Koch-Müller, M., Speziale, S., Deon, F., Mrosko, M., and Schade, U. (2011) Stress

708   induced proton disorder in hydrous ringwoodite. Physics and Chemistry of

709   Minerals, 38, 65-73.

710   Kohn, S.C., Brooker, R.V., Frost, D.J., Slesinger, A.E., and Wood, B.G. (2002)

711   Ordering of hydroxyl defects in hydrous wadsleyite (β-Mg_2SiO_4). American

712   Mineralogist, 87, 293-301.

713   Libowitzky, E. (1999) Correlation of O-H stretching frequencies and O-H…O

714   hydrogen bond lengths in minerals. Monatsh Chem, 130, 1047-1059.

715   Libowitzky, E., and Beran, A. (2006) The structure of hydrous species in nominally

716   anhydrous minerals: information from polarized IR spectroscopy. Review of

717   Mineralogy & Geochemistry, 62, 29-52.

718 Liu, J., Xia, Q.K., Kuritani, T., Hanski, E., and Yu, H.R. (2017) Mantle hydration and
719   the role of water in the generation of large igneous provinces. Nature
720   Communications, 8, 1824.

721 Liu, W.D., Yang, Y., Zhu, K., and Xia, Q.K. (2018) Temperatue dependecnes of
722   hydrous species in feldspars. Physics and Chemistry of Minerals,
723   https://doi.org/10.1007/s00269-018-0946-1.

724 Mackwell, S.J., Kohlstedt, D.L., and Paterson, M.S. (1985) The role of water in the
725   deformation of olivine single crystals. Journal of Geophysical Research, 90,
726   11319－11333.

727 Mackwell, S.J., and Kohlstedt, D.L. (1990) Diffusion of hydrogen in olivine:
728   implications for water in the mantle. Journal of Geophysical Research, 95,
729   5079-5088.

730 Nakamoto, K., Margosches, M., and Rundle, R.E. (1955): Stretching frequencies as a
731   function of distances in hydrogen bonds. Journal of the American Chemical
732   Society, 77, 6480-6486.

733 Padrón-Navarta, J.A., Hermann, J., and O'Neill, H.S.C. (2014) Site-specific hydrogen
734   diffusion rates in forsterite. Earth and Planetary Science Letters, 392, 100-112.

735 Pandolfo, F., Cámara, F., Domeneghetti, M.C., Alvaro, M., Nestola, F., Karato, S.,
736   and Amulele, G. (2015) Volume thermal expansion along the jadeite-diopside
737   join. Physics and Chemistry of Minerals, 42, 1-14.

738 Panero, W.R., Smyth, J.R., Pigott, J.S., Liu, Z., and Frost, D.J. (2013). Hydrous
739   ringwoodite to 5 K and 35 GPa: Multiple hydrogen bonding sites resolved with
740   FTIR spectroscopy. American Mineralogist, 98, 637-642.

741 Peslier, A.H., Woodland, A.B., Bell, D.R., and Lazarov, M. (2010) Olivine water
742   contents in the continental lithosphere and the longevity of cratons. Nature, 467,
743   78-U108.

26

744   Purevjav, N., Okuchi, T., Tomioka, T., Wang, X., and Hoffmann, C. (2016)
745   Quantitative analysis of hydrogen sites and occupancy in deep mantle hydrous
746   wadsleyite using single crystal neutron diffraction. Scientific Report, DOI:
747   10.1038/srep34988.

748   Purwin, H., Stalder, R., and Skogby, H. (2009) Hydrogen incorporation in Fe- and
749   Na-doped diopsides. European Journal of Mineralogy, 21(4), 691-704.

750   Padrón, J.A., and Hermann, J. (2017) A Subsolidus Olivine Water Solubility Equation
751   for the Earth's Upper Mantle. Journal of Geophysical Research: Solid Earth, DOI:
752   10.1002/2017JB014510.

753   Qin, T., Wentzcovitch R.M., Umemoto, K., Hirschmann, M.M., and Kohlstedt, D.L.
754   (2018) Ab initio study of water speciation in forsterite: Importance of the
755   entropic effect. American Mineralogist, 103, 692-699.

756   Rossi, G., Oberti, R., Dal, N.A., Molin, G.M., and Mellini, M. (1987) Residual
757   electron density at the M2 site in C2/c clinopyroxenes; relationships with bulk
758   chemistry and sub-solidus evolution. Physics and Chemistry of Minerals, 14,
759   514-520.

760   Sakurai, M., Tsujino, N., Tateno, S., Suzuki, T., Yoshino, T., Kawamura, K., and
761   Takahashi, E. (2015) In situ high pressure IR spectroscopic observations on the
762   upper mantle anhydrous minerals using diamond anvil cell. Japan Geoscience
763   Union Meeting.

764   Shuai, K., and Yang, X.Z. (2017) Quantitative analysis of H-species in anisotropic
765   minerals by polarized infrared spectroscopy along three orthogonal directions.
766   Contributions to Mineralogy and Petrology, 172, 14.

767   Skogby, H., and Rossman, G.R. (1989) OH⁻ in pyroxene: An experimental study of
768   incorporation mechanisms and stability. American Mineralogist, 74, 1059-1069.

769   Skogby, H., Bell, D.R., and Rossman, G.R. (1990) Hydroxide in pyroxene: variations
770   in the natural environment. American Mineralogist, 75, 767-774.

771   Smyth, J.R., Bell, D.R., and Rossman, G.R. (1991) Incorporation of hydroxyl in
772   upper-mantle clinopyroxenes. Nature, 351, 732-735.

773   Stalder, R., and Ludwig, T. (2007) OH incorporation in synthetic diopside. European
774   Journal of Mineralogy, 19(3), 373-380.

775   Thomas, S.M., Bina, C.R., Jacobsen, S.D., and Goncharov, A.F. (2012) Radiative heat
776   transfer in a hydrous mantle transition zone. Earth and Planteary Science Letters,
777   357, 130-136.

778   Thoraval, C., Demouchy, S., and Padrón, J.A. (2018) Relative diffusivities of hydrous
779   defects from partially dehydrated natural olivine. Physics and Chemistry of
780   Minerals. DOI: https://doi.org/10.1007/s00269-018-0982-x.

781   Tian, Z.Z., Liu, J., Xia, Q.K., Ingrin, J., Hao, Y.T., and Christophe, D. (2016) Water
782   concentration profiles in natural mantle orthopyroxenes: A geochronometer for
783   long annealing of xenoliths within magma. Geology, G38620.1

784   Tielke, J.A., Zimmerman, M.E., and Kohlstedt, D.L. (2017). Hydrolytic weakening in
785   olivine single crystals. Journal of Geophysical Research, 122, 3465-3479.

786   Tokawai, K., and Nakashima, S. (2010) Dehydration kinetics of muscovite by in situ
787   infrared microspectroscopy. Physics and Chemistry of Minerals, 37, 91-101.

788   Tollan PME, O'Neill HSC, Hermann J, Benedictus A, and Arculus RJ (2015) Frozen
789   melt-rock reaction in a peridotite xenolith from sub-arc mantle recorded by
790   diffusion of trace elements and water in olivine. Earth and Planetary Science
791   Letters, 422, 169-181.

792   Wang, D.J., Mookherjee, M., and Xu, Y.S. (2006) The effect of water on the electrical
793   conductivity of olivine. Nature, 443, 977-980.

794   Withers, A.C., and Behrens, H. (1999) Temperature-induced changes in the NIR
795   spectra of hydrous albitic and rhyolitic glasses between 300 and 100K. Physics
796   and Chemistry of Minerals, 27, 119-132.

797 Xia, Q.K., Liu, J., Liu, S.C., Kovács, I., Feng, M., and Dang, L. (2013) High water
798   content in Mesozoic primitive basalts of the North China Craton and implications
799   on the destruction of cratonic mantle lithosphere. Earth and Planetary Science
800   Letters, 361, 85-97.

801 Xu, H., Zhao, Y., Hickmott, D.D., Lane, N.J., Vogel, S.C., Zhang, J., and Daemen, L.L.
802   (2013) High-temperature neutron diffraction study of deuterated brucite. Physics
803   and Chemistry of Minerals, 40, 799-810.

804 Yang, X.Z., Xia, Q.K., Deloule, E., Dallai, L., Fan, Q.C., and Feng, M. (2008) Water
805   in minerals of the continental lithospheric mantle and overlying lower crust: A
806   comparative study of peridotite and granulite xenoliths from the North China
807   Craton. Chemical Geology, 256, 33-45.

808 Yang, X.Z., and Keppler, H. (2011) In-situ infrared spectra of OH in olivine to 1100℃.
809   American Mineralogist, 96, 451-454.

810 Yang, X.Z., and McCammon, C. (2012) Fe^{3+}-rich augite and high electrical
811   conductivity in the deep lithosphere. Geology, 2, 131-134.

812 Yang, X.Z., Keppler, H., Dubrovinsky, L, and Kurnosov, A. (2014) In-situ infrared
813   spectra of hydroxyl in wadsleyite and ringwoodite at high pressure and high
814   temperature. American Mineralogist, 99, 724-729.

815 Yang, Y., Xia, Q., Feng, M., and Zhang, P. (2010) Temperature dependence of IR
816   absorption of OH species in clinopyroxene. American Mineralogist, 95,
817   1439-1443.

818 Yang, Y., Xia, Q., Feng, M., and Gu, X.Y. (2011) In situ varying temperature FTIR
819   experiment study of rutile. American Mineralogist, 96, 1851-1855.

820 Yang, Y., Xia, Q., Feng, M., and Liu, S. (2012) OH in nature orthopyroxene: an in situ
821   FTIR investigation at varying temperatures. Physics and Chemistry of Minerals,
822   39, 413-418.

823 Yang, Y., Xia, Q., and Zhang, P. (2015) Evolutions of OH groups in diopside and

29

824   feldspars with temperature. European Journal of Mineralogy, 27, 185-192.

825   Yoshino, T., Matsuzaki, T., Yamashita, S., and Katsura, T. (2006) Hydrous olivine
826   unable to account for conductivity anomaly at the top of the asthenosphere.
827   Nature, 443, 973-976.

828   Yoshino, T., Manthilake, G., Matsuzaki, T., and Katsura, T. (2008) Dry mantle
829   transition zone inferred from the conductivity of wadsleyite and ringwoodite.
830   Nature, 451, 326-329.

831   Yoshino, T., and Katsura, T. (2013) Electrical conductivity of mantle minerals: role of
832   water in conductivity anomalies. Annual Review of Earth and Planetary Sciences,
833   41, 605-628.

834   Zhao, C.C., and Yoshino, T. (2016) Electrical conductivity of mantle clinopyroxene as
835   a function of water content and its implication on electrical structure of
836   uppermost mantle. Earth and Planetary Science Letters, 447, 1-9.

837   Zhang, M., Hui, Q., Lou, X.J., Redrern, S.A.T., Salje, E.K.H., and Tarantino, S.C.
838   (2006) Dehydroxylation, proton migration, and structural changes in heated talc:
839   An infrared spectroscopic study. American Mineralogist, 91, 816-825.

840   Zhang, M., Salje, E. K. H., Carpenter, M. A., Wang, J.Y., Groat, L. A., Lager, G. A.,
841   Wang, L., Beran, A., and Bismayer, U. (2007) Temperature dependence of IR
842   absorption of hydrous/hydroxyl species in minerals and synthetic materials.
843   American Mineralogist, 92, 1502-1517.

844   Zhang, M., Tarantino, S.C., Su, W., Lou, X., and Ren, X. (2016) Phonons, OH
845   vibrations ans structural modifications of phlogopite at high temperatures: an
846   in-situ infrared spectroscopic study. American Mineralogist, 101, 1873-1883.

847   **Figure captions**

848   FIGURE 1.Unpolarized FTIR spectra of OH in the ten clinopyroxenes at room

849   temperature. The spectra are shifted for clarity. The positions of the four groups OH

850   bands are indicated by dotted lines: red lines indicate the group 1 OH; blue lines

851   indicate the group 2 OH; green lines indicate the group 2 OH; black lines indicate the

852   group 4 OH.

853   FIGURE 2. Relationship between OH frequencies and chemical compositions in

854   the clinopyroxenes: (a) Wavenumbers of the group 1 OH band as a function of

855   tetrahedral coordinated Al^{3+} content in atoms per formula unit (a.p.f.u.). The data of

856   diopside (YT-25, peridotite) is from Hao et al. (2016), the data of diopside (NS-16,

857   peridotite) and diopside (NS-29, peridotite) are from Yang et al. (2008). The data of

858   augite and diopside (GRR04, granulite) are unpublished data; (b) Wavenumbers of the

859   group 2a OH band as a function of tetrahedral coordinated Al^{3+} content in atoms per

860   formula unit (a.p.f.u.); (c) Wavenumbers of the group 2b OH band as a function of M

861   vacancies; (d) Wavenumbers of the group 3 OH band as a function of M vacancies.

862   The M vacancy is a first approximation since the calculation is very simple neglecting

863   Fe^{3+}.

864   FIGURE 3. In situ unpolarized FTIR spectra of OH in the ten clinopyroxenes at

865   high temperatures. The room-temperature positions of the OH bands are indicated by

866   dotted lines. The arrow indicates the appearance of the new band at 3443 cm^{-1} in the

867   diopside-Austria and diopside-Aksu2. The spectra are shifted for clarity.

868   FIGURE 4. Plots of frequency of the OH bands of clinopyroxenes against

869   temperature: (a) group 1; (b) group 2a; (c) group 2b; (d) group 3; (e) group 4

870   FIGURE 5. Variation of the integral absorbances of the OH bands with

871   temperature: (a) The bulk integral absorbances; (b) The individual integral absorbance

872   of each OH band. The dotted lines indicate the turning points at which dehydration

873   starts.

874   FIGURE 6. Room-temperature unpolarized FTIR spectra of the samples

875   annealed in N_2 at $1000^{o}C$.

876   FIGURE 7. Hydrogen diffusivities during dehydration as a function of Fe and

877   [IV]Al content in atoms per formula unit (a.p.f.u.): (a) Bulk and site-specific hydrogen

878   diffusivities vs. Fe content; (b) Bulk and site-specific hydrogen diffusivities vs. [IV]Al

879   content; (c) Bulk hydrogen diffusivities vs. Fe content excluding the diopside-Austria;

880   (d) Bulk hydrogen diffusivities vs. [IV]Al content excluding the diopside-Austria.

881   FIGURE 8. Unpolarized NIR spectra of the samples normalized to 1 cm of

882 thickness before and after dehydration. The arrows indicate the absorptions of Fe^{2+}.

883   FIGURE 9. (a) Relationship between temperature dependence of OH frequency

884 shift and room-temperature frequency. The blue symbols are the data from this study

885 and the black symbols are the data from the literature. (b) Correlation between O-H

886 stretching frequency and O-H…O distance of the four groups of OH. The black

887 symbols indicate the data at room temperature, and the blue symbols indicate the data

888 at 1000 $^{\circ}$C. For each group of OH in the ten samples, the highest and lowest

889 frequencies were chosen. (c) The comparison of ranges of O-H…O distance of the

890 four groups of OH between room temperature and 1000 $^{\circ}$C.

891   FIGURE 10. (a) Unpolarized FTIR spectra of OH in the diopside from Austria

892 recorded at room temperature before heating and after annealing at 800 and 900 $^{\circ}$C for

893 different time. The dotted lines indicate the new band at 3443 cm^{-1}. The spectra are

894 shifted for clarity. (b) Room-temperature polarized FTIR spectra of OH in diopside

895 from Austria after annealing at 900 $^{\circ}$C for 30 min with polarizer rotating 0° and 90°. (c)

896 Plots of integral absorbance of the deconvoluted OH bands of the diopside from

897 Austria against annealing time at 800 $^{\circ}$C (integral absorbance of the FTIR spectrum

898 before heating was used as the initial value). (d) Integral absorbance of the

899 deconvoluted OH bands of the diopside from Austria against annealing time at 900

900 $^{\circ}$C.

901

902

903

904

905

906

32

907 **Table 1** Cation proportions as calculated from electron microprobe analyses of

908 clinopyroxenes.

	Diopside-Austria	Diopside-marble	Diopside-JD	Augite-YFL	Omphacite	Diopside-Aksu	Diopside-Russia	Diopside-deep sea	Augite-NS
K	0.000	0.000	0.000	0.000	0.000	0.000	0.000	0.000	0.000
Na	0.003	0.001	0.135	0.119	0.232	0.001	0.023	0.033	0.122
Cr	0.000	0.000	0.023	0.000	0.002	0.000	0.017	0.033	0.000
Ca	0.992	1.010	0.776	0.653	0.676	1.016	0.952	0.871	0.648
Mg	0.888	0.896	0.782	0.706	0.717	0.929	0.930	0.828	0.818
Mn	0.006	0.003	0.003	0.004	0.002	0.004	0.001	0.002	0.003
Ti	0.001	0.003	0.014	0.030	0.003	0.000	0.003	0.005	0.023
Al	0.011	0.088	0.301	0.469	0.185	0.009	0.009	0.298	0.389
Ni	0.001	0.001	0.002	0.001	0.002	0.001	0.001	0.000	0.000
Fe	0.076	0.043	0.089	0.300	0.195	0.072	0.043	0.085	0.223
Si	2.000	1.955	1.883	1.756	2.002	1.982	2.009	1.846	1.808
Total	3.978	4.000	4.008	4.038	4.016	4.014	3.988	4.001	4.034
^{IV}Al	0.000	0.045	0.117	0.244	0.000	0.018	0.000	0.154	0.192
^{VI}Al	0.011	0.043	0.184	0.225	0.185	-0.009	0.009	0.144	0.197
Vacancies	0.022	0.000	-0.008	-0.038	-0.016	-0.014	0.012	-0.001	-0.034

909 Note: The total Fe was calculated as FeO. The error of multi-point analysis is <1% for elements

910 with concentration >5% and <3% for elements with concentration >1%. The cations were

911 calculated based on 6 oxygen atoms except for the data for diopside (marble) which were from

912 Johnson et al. (2002). The vacancies were calculated as 4 minus total cations per 6 oxygen atoms.

913 The diopside-Aksu1 and diopside-Aksu2 have the same chemical composition, labeled as

914 diopside-Aksu in the table.

915

916

917

918

919

920

921

922

923 **Table 2** Bulk and site-specific hydrogen diffusivities

Sample	Thickness (mm)	Temperature (°C)	Site-specific diffusivity ($\log_{10}D$)						Bulk diffusivity ($\log_{10}D$)
			Peak position (cm^{-1})						
			3640	3620	3540	3520	3450	3360	
Diopside-Russia	0.866	1000	-12.40 ±0.60	-12.15 ±0.54	/	-12.10 ±0.30	-12.15 ±0.54	/	-12.15 ±0.24
Diopside-marble	0.212	1000	-12.30 ±0.30	/	-12.00 ±0.22	/	/	/	-12.22 ±0.18
Diopside-JD	0.166	1000	-11.80 ±0.20	/	-11.92 ±0.22	/	-11.74 ±0.18	/	-11.92 ±0.18
Diopside-deep sea	0.146	1000	-11.70 ±0.30	/	-12.00 ±0.22	/	-11.74 ±0.18	/	-12.00 ±0.26
Augite-NS	0.980	1000	-11.30 ±0.30	/	-11.10 ±0.20	/	-11.52 ±0.48	/	-11.22 ±0.18
Diopside-Austria	0.759	1000	-10.60 ±0.22	/	/	/	-10.70 ±0.30	-10.55 ±0.19	-10.80 ±0.20

924

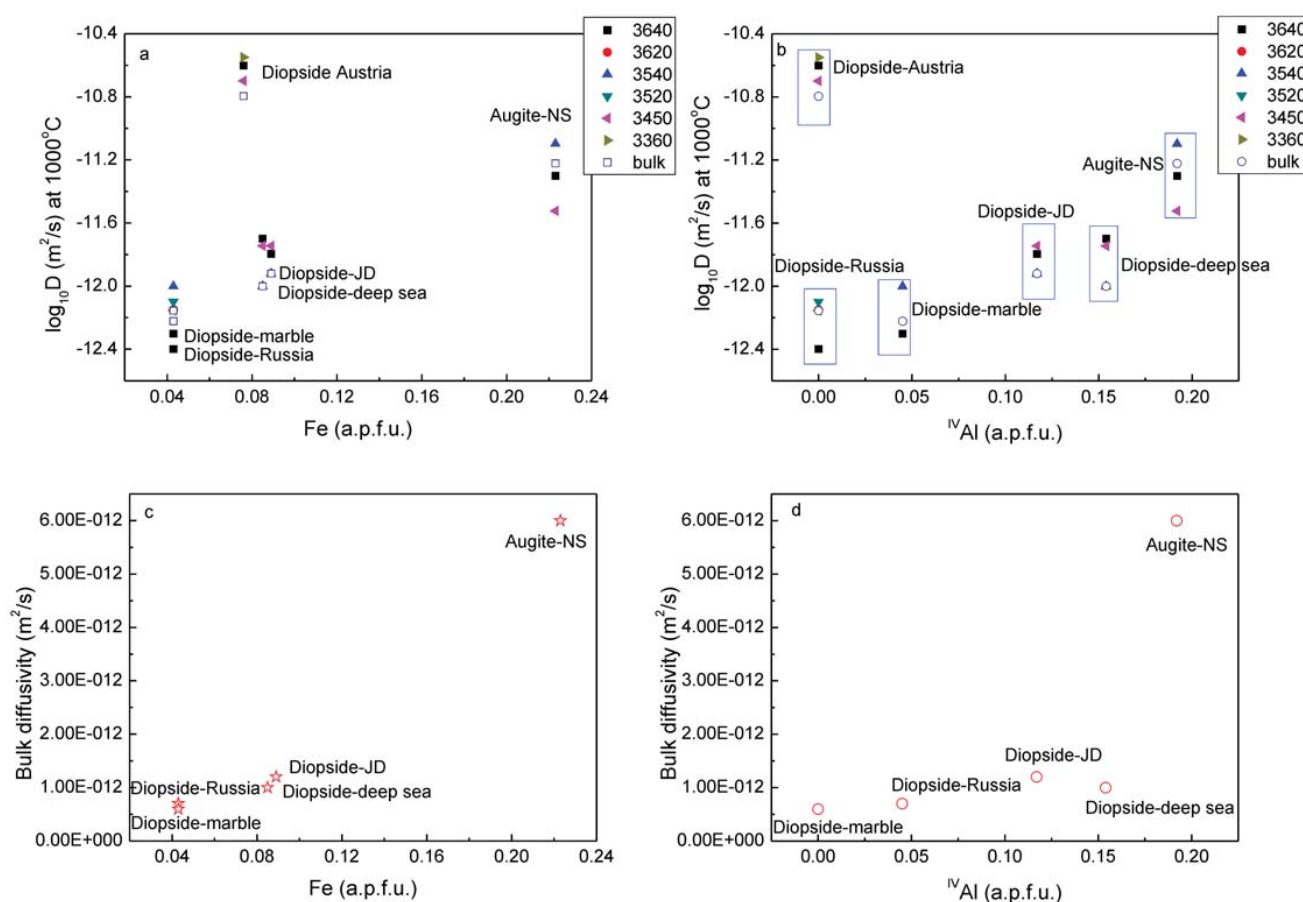925

34
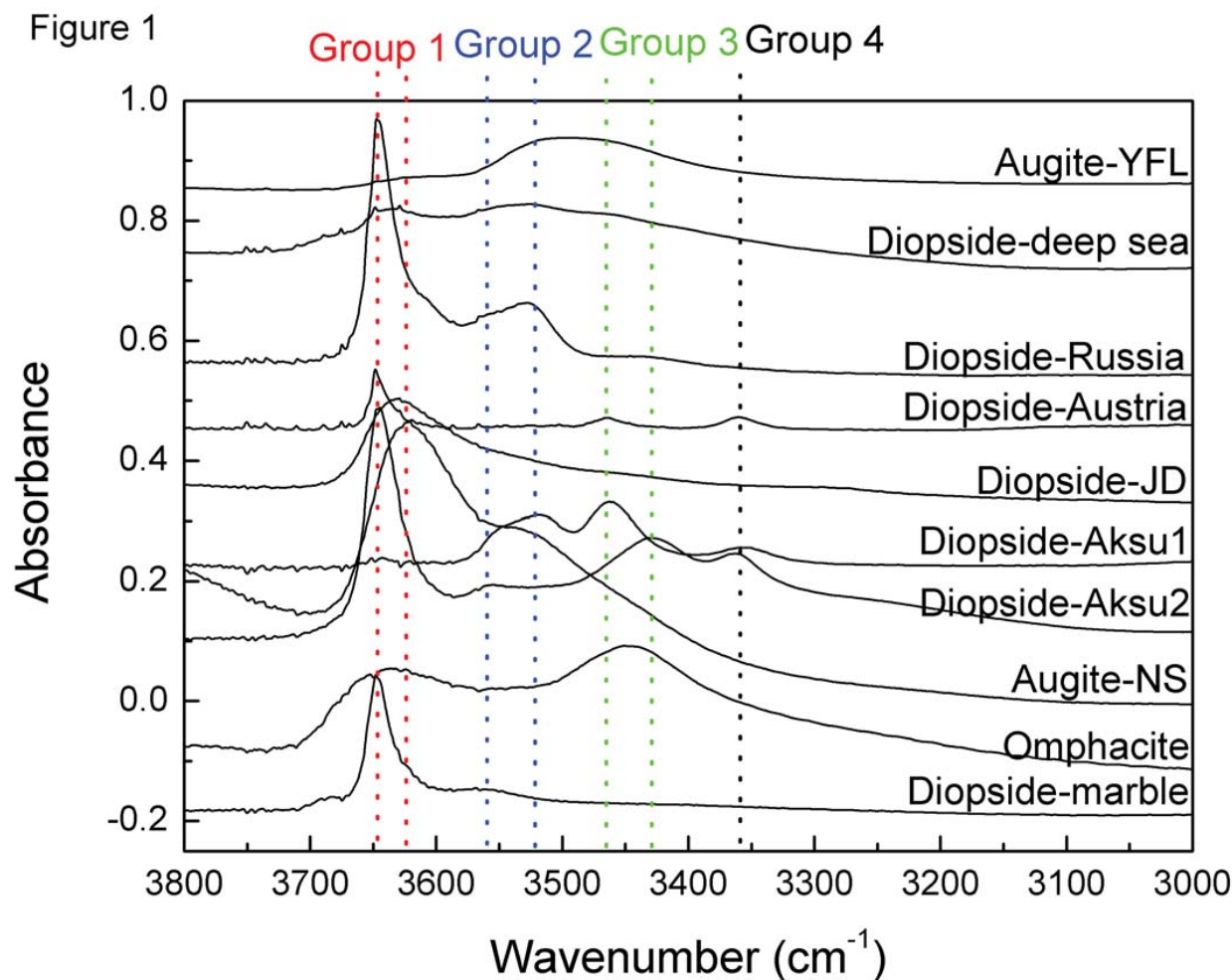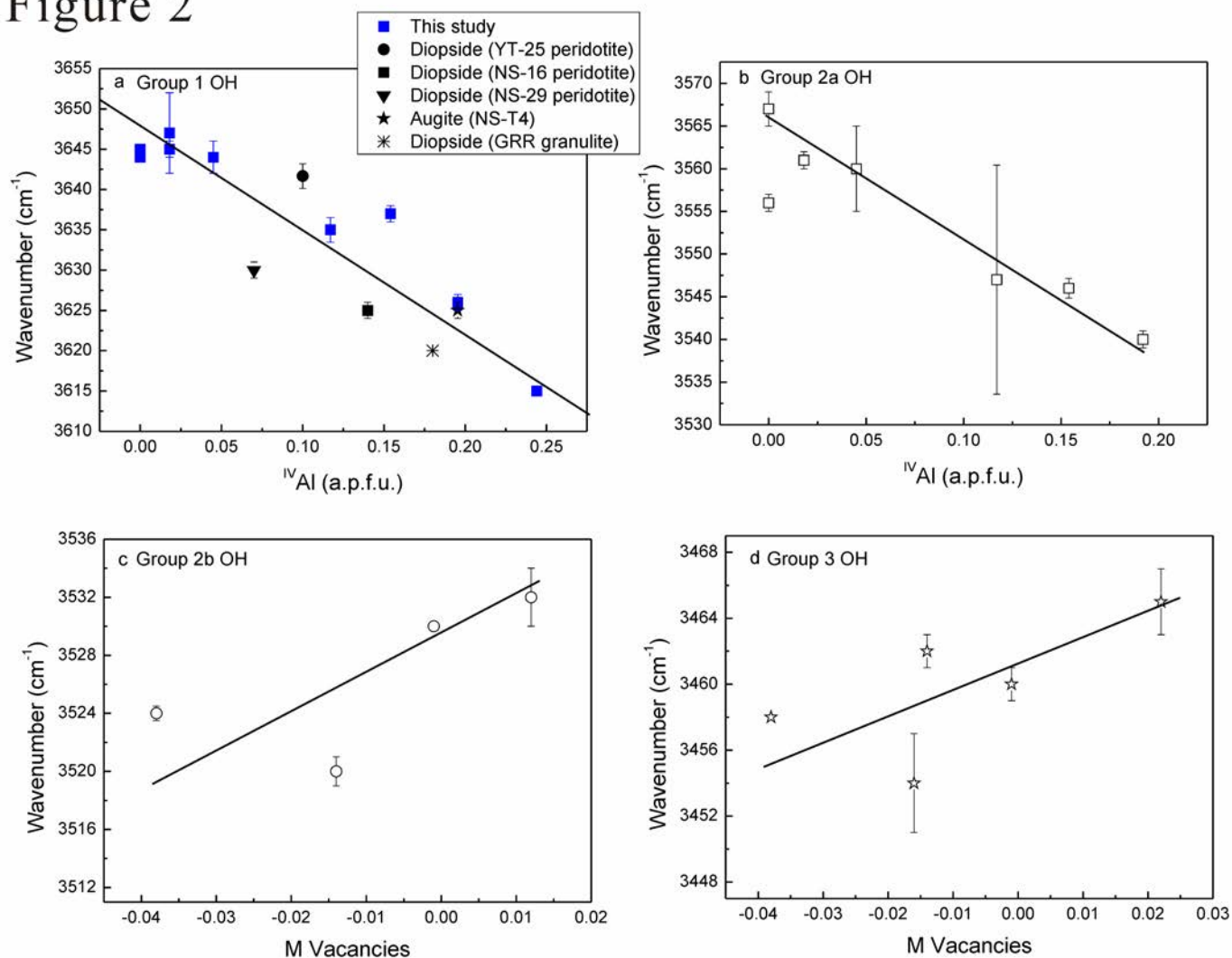
Figure 1
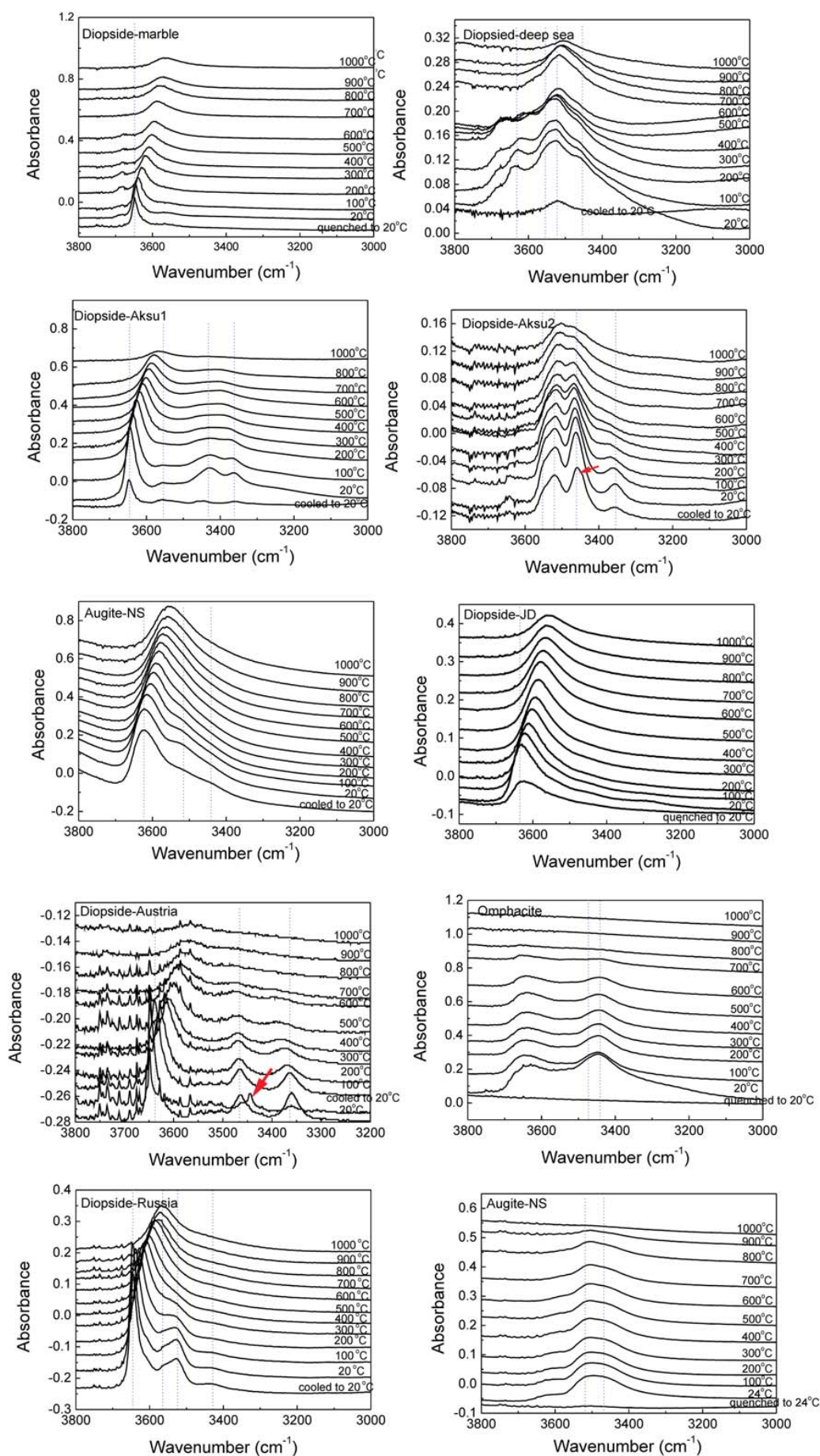
Figure 2

Figure 3

Figure 4
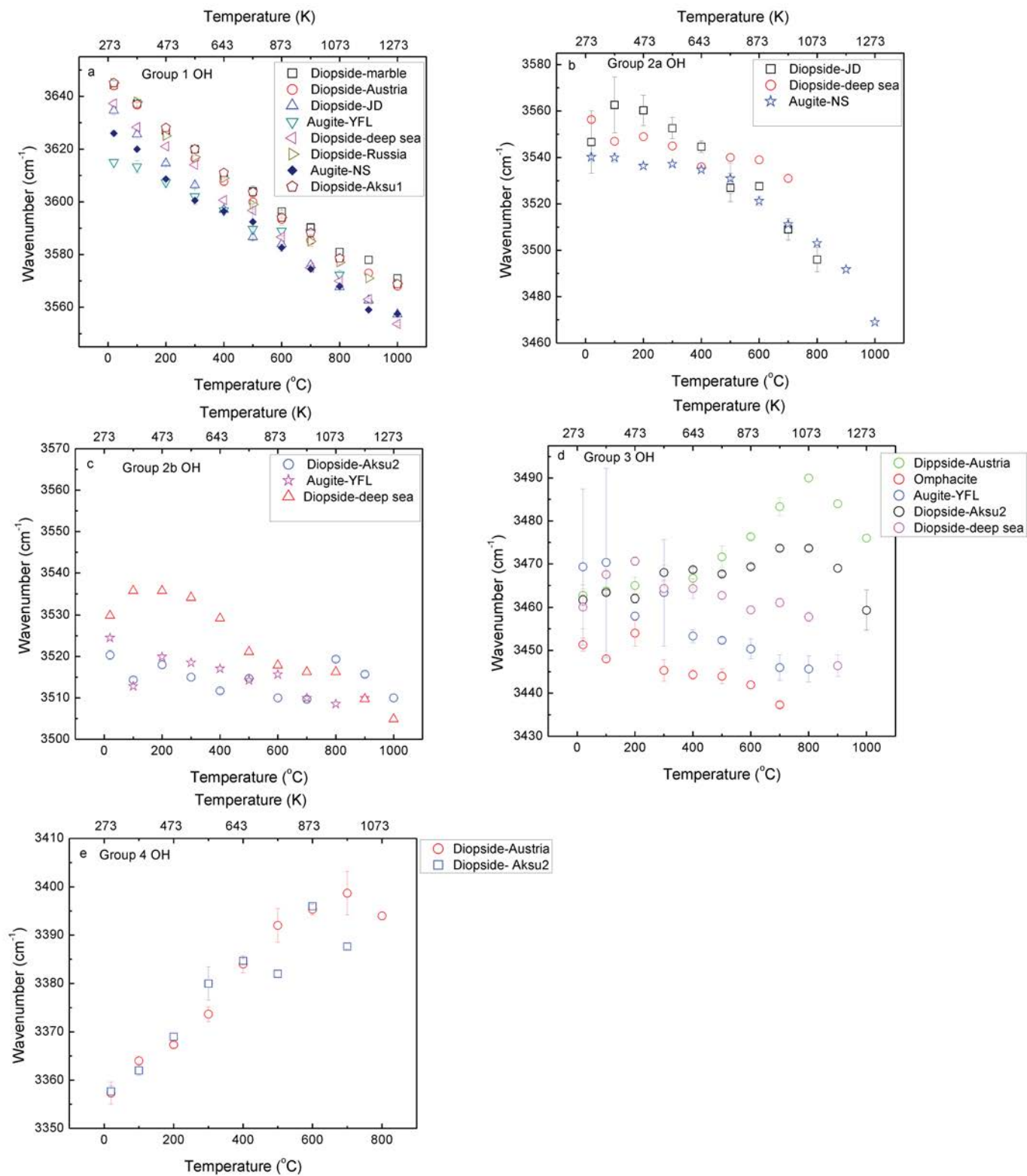
Figure 5
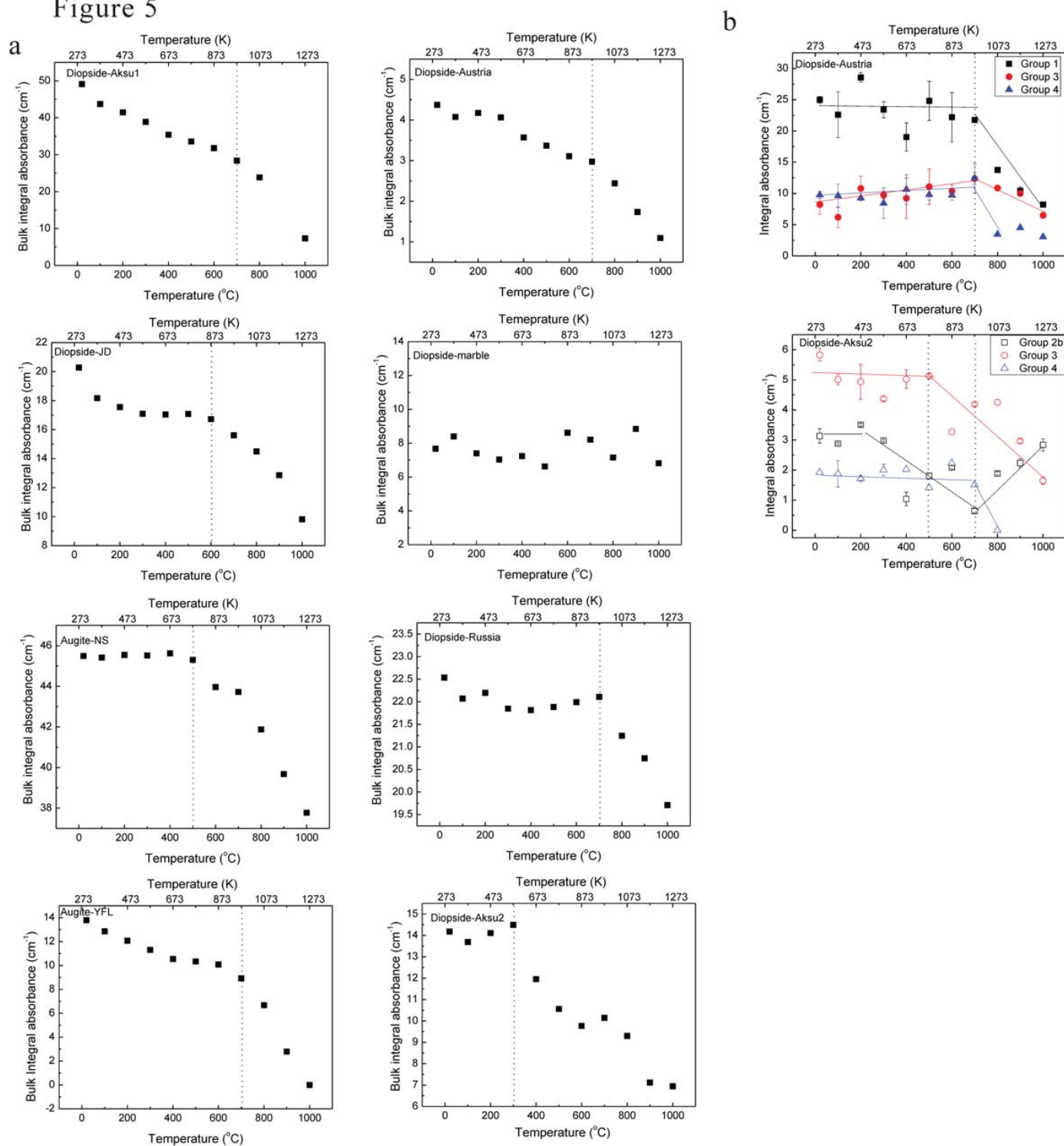
Figure 6
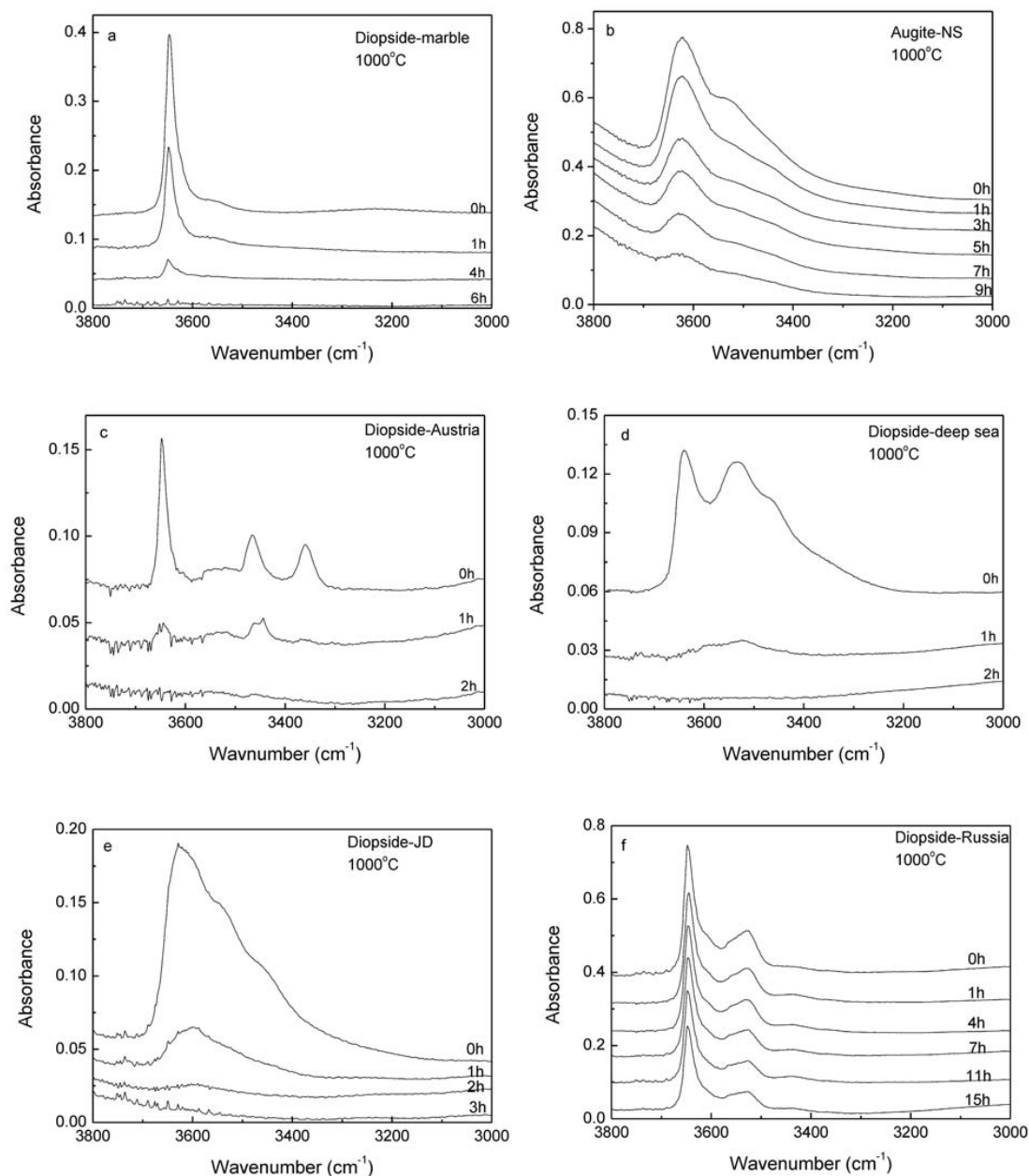
Figure 7

Figure 8

Figure 9

Figure 10